Urolithiasis (2023) 51:57
https://doi.org/10.1007/s00240-023-01425-7

RESEARCH

Epitranscriptomic profiling of m6A RNA methylation in renal epithelial tubular cells stimulated with calcium oxalate crystals through microarray analysis

Bo-Yu Yang[1] · Fang-Zhou Zhao[1] · Jun Li[1] · Xiao-Chuan Wang[1] · Hui-Min Zhao[1] · Ye Tian[1]

Received: 19 March 2022 / Accepted: 27 February 2023 / Published online: 22 March 2023

Abstract

The aim of this study was to investigate the relationship of m6A RNA methylation to CaOX-induced renal tubular injury. Microarray analysis was performed to detect the difference in mRNA expression and m6A methylation between the injurious groups and controls. We established injurious renal tubular epithelial cell model induced by calcium oxalate crystals (CaOX), and we validated that CaOX could increase the overall m6A methylation levels. By microarray analysis, we identified 5967 differentially expressed mRNAs (2444 were up-regulated and 3523 were down-regulated in the injurious groups) and 6853 differentially methylated mRNAs (4055 were in hypermethylation and 3688 were in hypomethylation in the injurious groups). Four clusters (hyper-up, hyper-down, hypo-up and hypo-down) were further identified via conjoint analysis. Functional analysis revealed that m6A methylation played a crucial role in the development of CaOX through participating multiple processes covering inflammation, oxidative stress, apoptosis, crystal–cell adhesion. We delineated the first transcriptome-wide m6A landscape of injurious renal tubular cells in high-CaOX environment. We identified a series of mRNAs of renal tubular epithelial cells with differential expression and m6A methylation between the CaOX-treated groups and controls.

Keywords Nephrolithiasis · Calcium oxalate · m6A modification · N6-Methyladenosine

Introduction

Nephrolithiasis is a common metabolic disease and its prevalence in all age groups is on the rise worldwide [1]. Calcium oxalate (CaOX) crystals, which are the main ingredient of kidney stones, can lead to intrarenal inflammatory response and oxidative stress injury, and consequentially facilitate crystal aggregation, adhesion and stone formation [2]. Alleviating CaOX-induced injury of renal tubular epithelial cells has been identified as a promising strategy for the treatment of nephrolithiasis [3, 4]. However, the pathological process of crystal–cell interaction has not been well elucidated.

N6-methyladenosine (m6A) represents the most prominent internal RNA modification in eukaryotes [5]. m6A is a dynamic reversible post-transcriptional modifying process, which is regulated by methyltransferases (writers), demethylases (erasers) and recognition proteins (readers) [6]. The m6A labels can affect the fate of methylated RNAs via regulating its splicing, nuclear export, decay and translation [7]. It has been demonstrated that aberrant m6A methylation is crucial for the development of multiple human diseases, such as cancer, cardiovascular and brain diseases [8–10].

Bo-Yu Yang and Fang-Zhou Zhao contributed equally to this work.

✉ Jun Li
zfzlijun@126.com

Bo-Yu Yang
ybyurology@163.com

Fang-Zhou Zhao
zfz1501112@163.com

Xiao-Chuan Wang
776308874@qq.com

Hui-Min Zhao
1459913619@qq.com

Ye Tian
tianyouyiyiyuan@163.com

[1] Department of Urology, Capital Medical University Affiliated Beijing Friendship Hospital, Beijing 100050, China

But so far, little progress has been made to investigate the relationship of m6A regulation to CaOX-induced renal tubular injury and stone formation. In our study, we selected human kidney proximal tubular cells (HK-2) as models due to its major role of oxalate handling [11], and delineated the first m6A methylation landscape of injurious HK-2 cells in high-CaOX environment via microarray analysis. This study firstly uncovered the pathophysiological process of crystal–cell interaction from the perspective of epigenomics.

Methods

Cell culture and CaOX exposure

HK-2 cell line was cultured in DMEM supplemented with 10% fetal bovine serum (FBS) in an incubator at 37 °C with 5% CO2. Commercial calcium oxalate monohydrate crystals were purchased from Sigma Aldrich (C0350000, USA). The adherent cells were treated with CaOX suspension at a concentration of 100 μg/mL for 24 h, and these conditions had been proven to be effective to induce oxidative stress injury [3]. Finally, RNA was collected for microarray sequencing.

Lactate dehydrogenase (LDH) release

HK-2 cells were seed into 96-well plates (5×10^3 cells/well). After receiving the appropriate treatments, the medium was collected and centrifuged to remove crystals and cellular debris. We measured the absorbance of culture medium at 450 nm as the results of LDH activity. The detailed process could be consulted in the instructions of LDH Activity Assay Kit (Solarbio).

Tunel assays

HK-2 cells were seed into cell climbing films and treated after adherence as mentioned above. And then, cell films were put into 4% paraformaldehyde for cell fixation. After enhancing membrane permeability, we added TdT Enzyme reaction solution and Streptavidin-TRITC as instructed by One-step TUNEL Cell Apoptosis Detection Kit (KeyGEN). Relative cell apoptosis was assessed with fluorescence microscope.

RNA extraction and quantitative real-time PCR (qRT-PCR)

Total RNA was extracted by TRIzol™ Reagent and then reverse transcribed using the *TransScript*® First-Strand cDNA Synthesis SuperMix (TransGen). qPCRs were conducted on Applied Biosystems 7500 system with *TransStart*® Green qPCR SuperMix (TransGen). Gene expression was normalized to GAPDH.

Measurement of m6A levels

The m6A levels were measured using EpiQuik m6A RNA Methylation Quantification Kit according to the manufacturer's instructions (Epigentek). In addition, we added the m6A Dot Blot assays to validate the reliability. The 2 μg total RNAs were spotted onto a nylon membrane, and then incubated with m6A antibody (A19841, ABclonal) at 4 °C overnight. The m6A dots were analyzed using an imaging system (Bio-Rad).

Western blot

Cells were washed with PBS and lysed with RIPA buffer. An equal amount of protein was separated by SDS-PAGE and then transferred to PVDF membrane, and blotted with related antibodies in 4 °C overnight. HRP-labeled secondary antibody for 2 h at room temperature and protein bands were revealed by enhanced chemiluminescence (ECL). Antibodies used in this study were purchased from Abcam: rabbit anti-METTL3 antibody (ab195352), rabbit anti-METTL14 antibody (ab98166), rabbit anti-ALKBH5 antibody (ab195377); Cell Signaling Technology: rabbit anti-WTAP antibody (#56,501); ABclonal: rabbit anti-FTO antibody (A1438).

m6A Immunoprecipitation

3–5 μg total RNA and m6A spike-in control mixture were added to 300 μL 1 × IP buffer containing 2 μg anti-m6A rabbit polyclonal antibody (Synaptic Systems). The reaction was incubated with head-over-tail rotation at 4 °C for 2 h. 20 μL Dynabeads™ M-280 Sheep Anti-Rabbit IgG suspension per sample was blocked with freshly prepared 0.5% BSA at 4 °C for 2 h, washed three times with 300 μL 1 × IP buffer, and resuspended in the total RNA-antibody mixture prepared above. The RNA binding to the m6A-antibody beads was carried out with head-over-tail rotation at 4 °C for 2 h. The beads were then washed three times with 500 μL 1 × IP buffer and twice with 500 μL Wash buffer. The enriched RNA was eluted with 200 μL Elution buffer at 50 °C for 1 h. The RNA was extracted by acid phenol–chloroform and ethanol precipitated.

Labeling and hybridization

The "IP" RNAs and "Sup" RNAs were added with equal amount of calibration spike-in control RNA, separately amplified and labeled with Cy3 (for "Sup") and Cy5 (for "IP") using Arraystar Super RNA Labeling Kit. 2.5 μg of

Cy3 and Cy5 labeled cRNAs were mixed. The cRNA mixture was fragmented by adding 5 μL 10 × Blocking Agent and 1 μL of 25 × Fragmentation Buffer, heated at 60 °C for 30 min, and combined with 25 μL 2 × Hybridization buffer. 50 μL hybridization solution was dispensed into the gasket slide and assembled to the m6A-mRNA&lncRNA Epitranscriptomic Microarray slide. The slides were incubated at 65 °C for 17 h in an Agilent Hybridization Oven. The hybridized arrays were washed, fixed and scanned using an Agilent Scanner G2505C.

Statistical analysis

Agilent Feature Extraction software was used to analyze acquired array images. Raw intensities of IP (immunoprecipitated, Cy5-labeled) and Sup (supernatant, Cy3-labeled) were normalized with average of log2-scaled Spike-in RNA intensities. After Spike-in normalization, the probe signals having Present (P) or Marginal (M) QC flags in a certain proportion were retained for further "m6A quantity" analyses. "m6A quantity" was calculated for the m6A methylation amount based on the IP (Cy5-labeled) normalized intensities. Differentially m6A-methylated mRNAs based on "m6A quantity" passing fold change and statistical significance cutoffs were identified and compiled. Differentially m6A-methylated RNAs and differentially expression genes between two groups were identified by filtering with fold change > 2 and $p < 0.05$. And then, GO enrichment and KEGG pathway enrichment analyses of these genes were performed, respectively, to explore their molecular function. By conjoint analysis, four classifications were identified and named with methylation status (hyper or hypo)-expression status (up-down). Hierarchical clustering was performed using the R software.

Results

CaOX crystals dysregulated the expression of m6A regulators and overall m6A levels of renal tubular epithelial cells

We utilized HK-2 cell line co-incubated with CaOX crystals to simulate the injurious renal tubular epithelial cells in high-CaOX environment. TUNEL and LDH release assays proved that the cell model was successfully established (Fig. 1A, B). We firstly determined whether CaOX crystals enabled to change its overall m6A levels via Dot blot and fluorometric methods. The results consistently showed that CaOX increased intracellular m6A methylation levels (Fig. 1C, D). To further explore whether m6A variations were affected by dysregulated expression of m6A regulators, we focused on three writers (METTL3, METTL14 and WTAP) and two erasers (FTO and ALKBH5), who played a major role in installing and removing m6A labels. The qPCR results showed that FTO and METTL3 were down-regulated when stimulated by CaOX crystals, and WTAP was significantly up-regulated (Fig. 1E). Western blots demonstrated

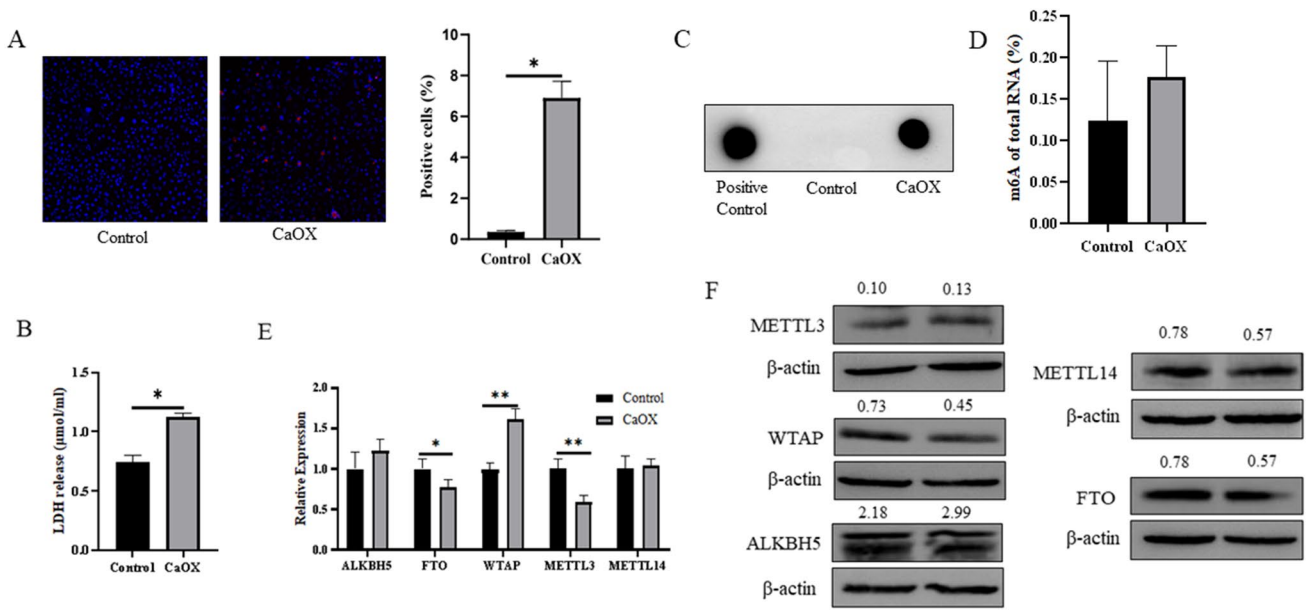

Fig. 1 CaOX crystals induced renal tubular cellular injury and increased overall m6A levels. Cellular injury was measured using TUNEL assays (**A**) and LDH release (**B**). Overall m6A levels were measured using Dot Blot (**C**) and EpiQuik m6A RNA Methylation Quantification Kit (**D**). The expression of three writers (METTL3, METTL14 and WTAP) and two erasers (FTO and ALKBH5) was detected by qPCR (**E**) and Western Blot (**F**)

that FTO, METTL14 and WTAP were all down-regulated in stimulated cells (Fig. 1F). This section indicated that the regulation of m6A methylation might be influenced by CaOX stimulation and m6A was involved in the process of crystal–cell interaction.

Differentially expressed mRNAs were identified between the injurious group and controls

Volcano plot demonstrated that a total of 5967 DEGs were screened out, of which 2444 were up-regulated and 3523 were down-regulated in the injurious groups (Fig. 2A). Hierarchical clustering and Functional enrichment analysis showed that up-regulated genes were mainly distributed in intracellular organelle and involved in cellular macromolecule metabolic process, regulation of cellular metabolic process and biosynthetic process (Fig. 3, Supplement Figure 1 and Supplement Table 1). In contrast, down-regulated genes were mainly distributed in cytoplasm and participated in cellular metabolic process, organonitrogen compound metabolic process and transport. Pathway analysis revealed that up-regulated genes were enriched in Herpes simplex virus 1 infection, Thyroid hormone signaling pathway and Ubiquitin-mediated proteolysis, while down-regulated genes were mainly enriched in ribosome, Huntington disease, NAFLD and oxidative phosphorylation (Fig. 4 and Supplement Table 2).

Differentially methylated mRNAs were identified between the injurious group and controls

To further depict RNA methylated profiling, m6A quantity, sites and percentage of total 37,015 transcripts were identified via microarray analysis. 6853 differentially methylated transcripts were selected based on the filter conditions described in Methods, among which 4055 were in hypermethylation and 3688 were in hypomethylation in the injurious groups (Fig. 2B). Surprisingly, functional analysis revealed that hypermethylated genes were also mainly distributed in intracellular organelle and involved in cellular macromolecule metabolic process and regulation of cellular metabolic process as DEGs, while hypomethylated genes were mainly distributed in cytoplasm and participated in location, organonitrogen compound metabolic process, establishment of location and transport (Fig. 5, Supplement Figure 2 and Supplement Table 3). Besides those biologic processes, we found that differentially methylated genes were also associated with cellular response to stress, cell cycle and oxidation–reduction process, which represented its preventive response to crystalline injury. Pathway analysis showed that hypermethylated genes were also mainly enriched in Herpes simplex virus 1 infection, Fanconi anemia pathway and apoptosis, while hypomethylated genes were enriched in systemic lupus erythematosus and apoptosis (Fig. 6 and Supplement Table 4).

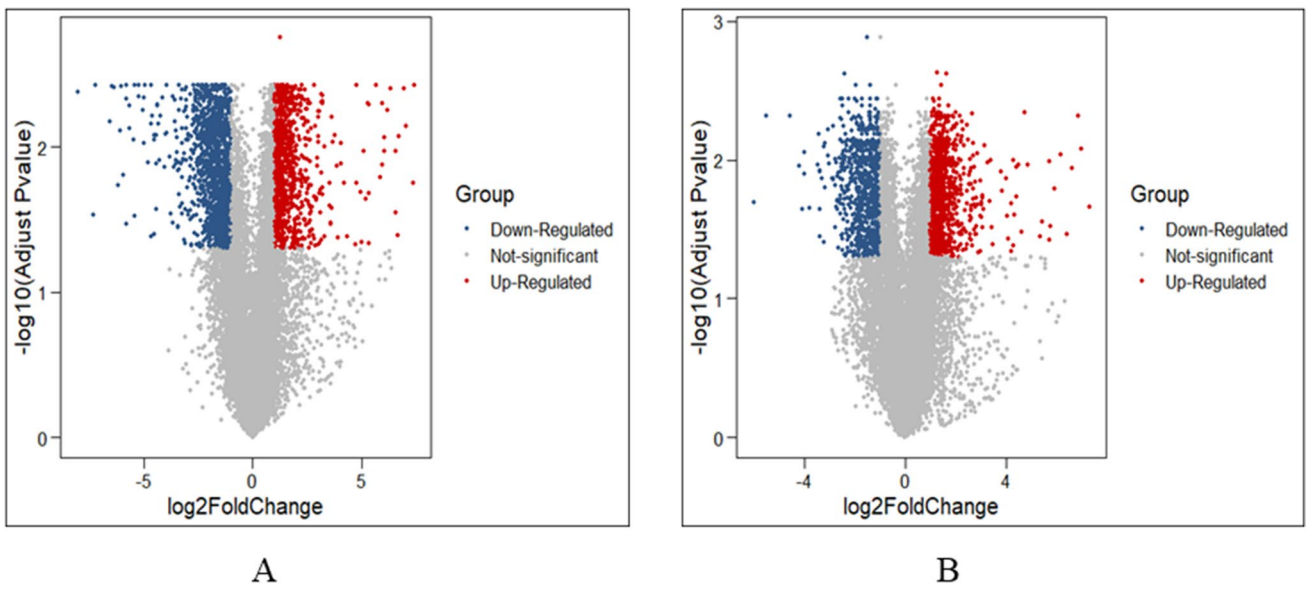

Fig. 2 Differentially expressed mRNAs and methylated mRNAs were identified between the injurious group and controls. (**A**) Differentially expressed genes. (**B**) Differentially methylated genes

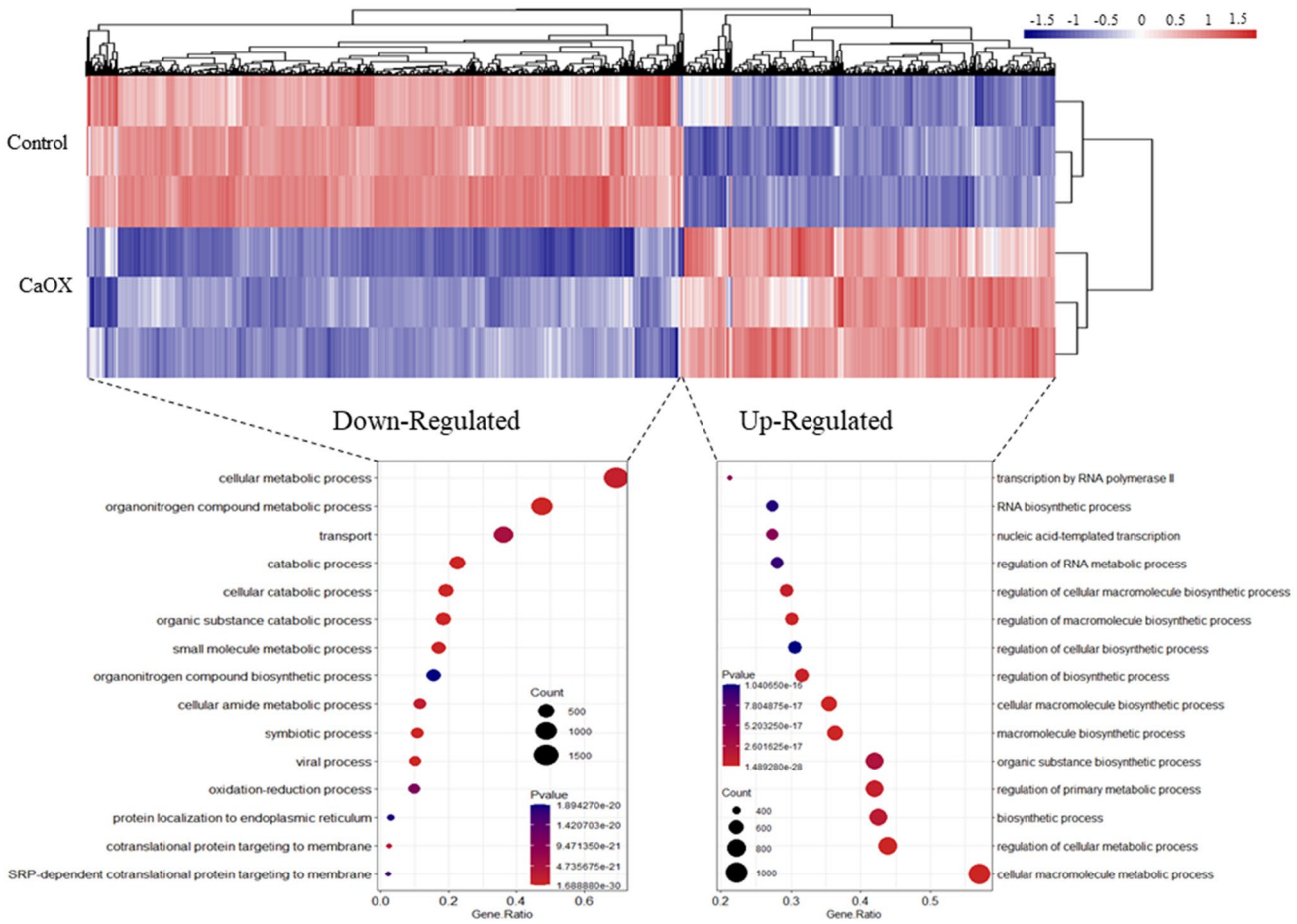

Fig. 3 Heatmap and dot plots showed the results of GO analysis of differentially expressed mRNAs

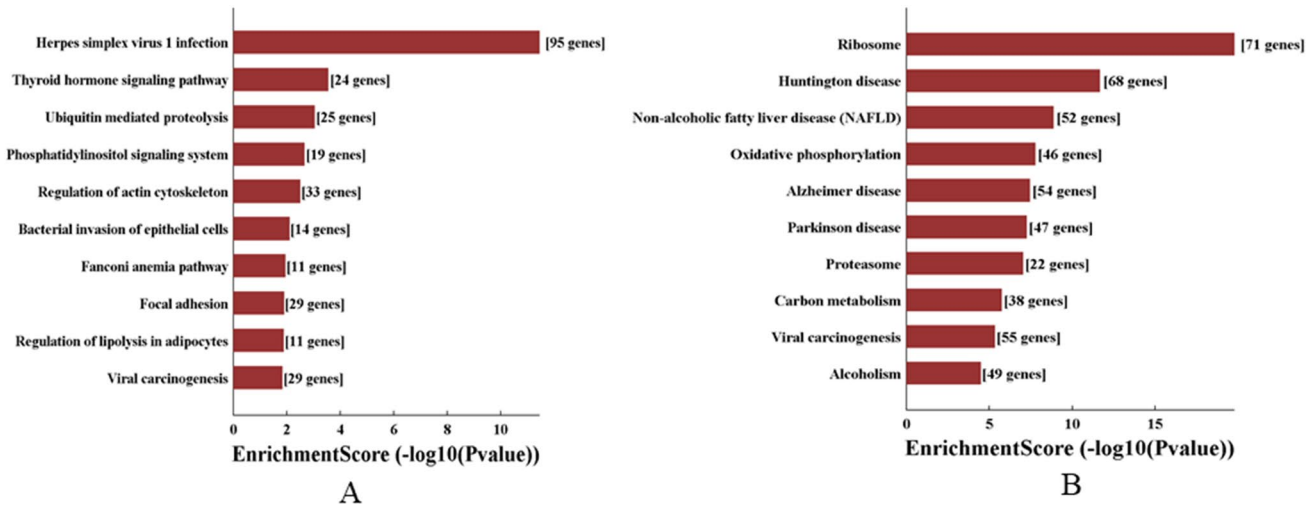

Fig. 4 Bar plots showed the enriched pathways in KEGG analysis of differentially expressed mRNAs

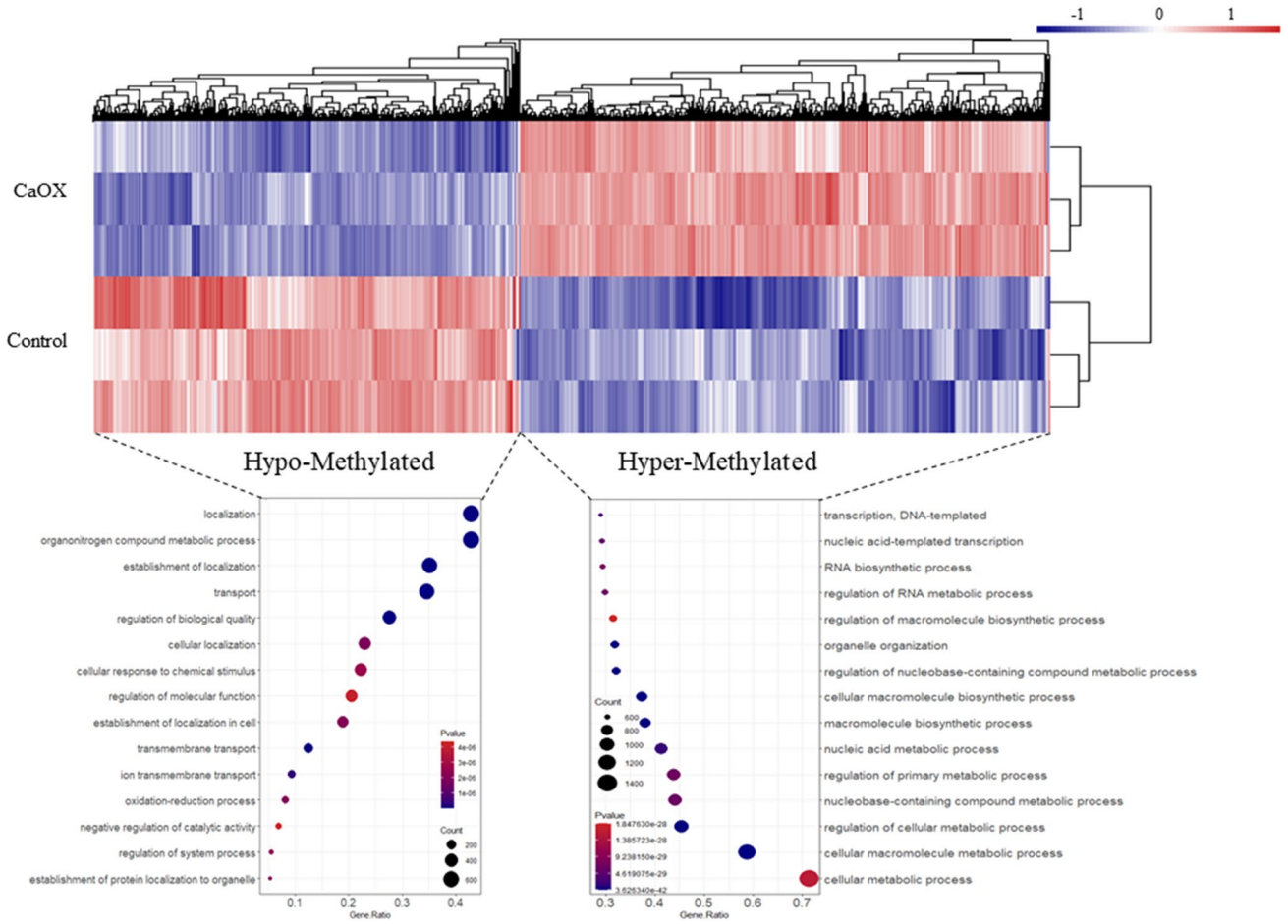

Fig. 5 Heatmap and dot plots showed the results of GO analysis of differentially methylated mRNAs

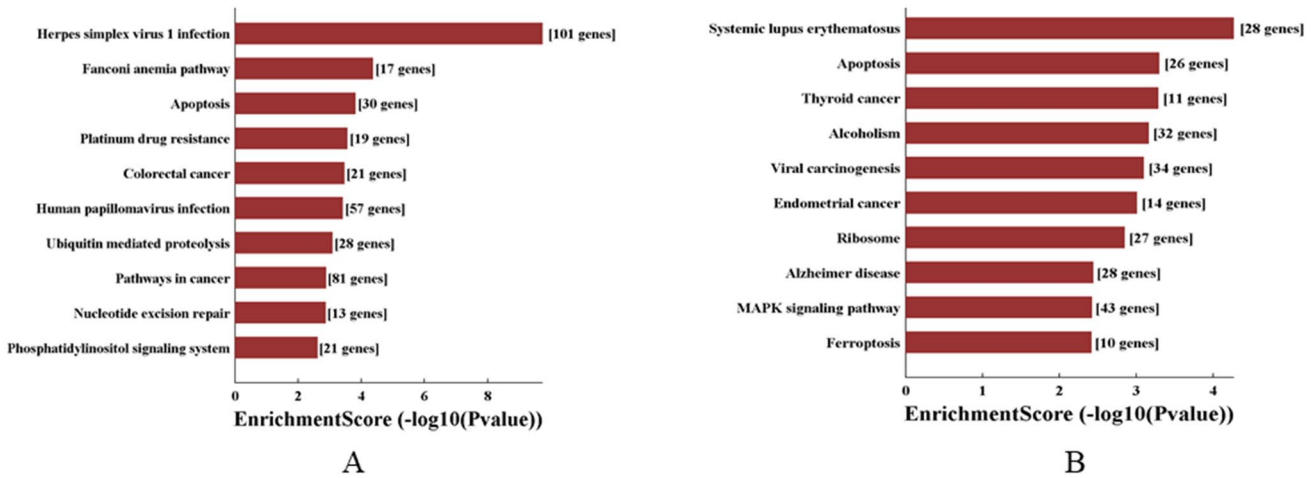

Fig. 6 Bar plots showed the enriched pathways in KEGG analysis of differentially methylated mRNAs

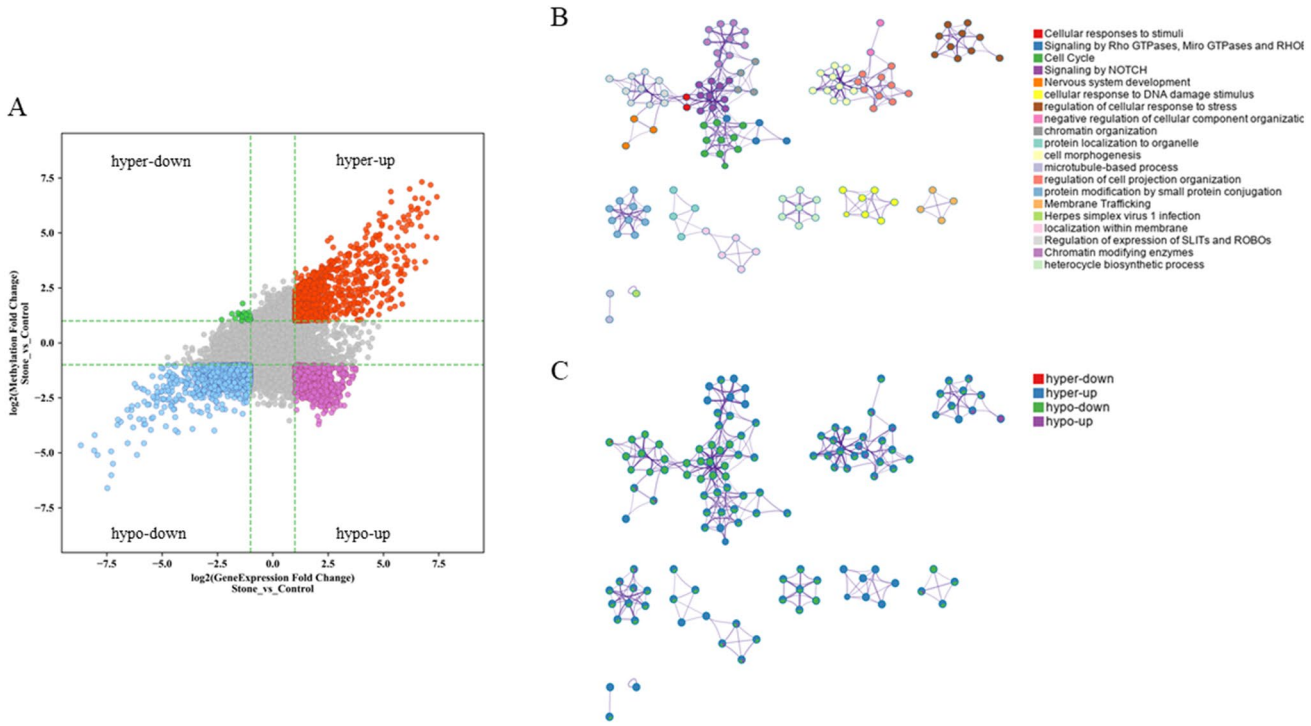

Fig. 7 Conjoint analysis identified four clusters and representative functional enrichment. (**A**) The 4-quadrant identified four classifications (hyper-up, hyper-down, hypo-up and hypo-down). (**B**) and (**C**) selected a subset of representative terms from the full cluster and converted them into a network layout. More specifically, each term is represented by a circle node, where its size is proportional to the number of input genes fall under that term, and its color represent its cluster identity (nodes of the same color belong to the same cluster)

Conjoint analysis of differentially m6A methylation and differentially gene expression

We performed a combined analysis to identify the underlying differentially expressed mRNAs regulated by m6A dynamic modification. The 4-quadrant results demonstrated that 1663 up-regulated and 20 down-regulated mRNAs were in hypermethylation status, while 674 up-regulated and 1140 down-regulated mRNAs were in hypomethylation status (Fig. 7 and Supplement Table 5). The top 10 m6A foldchange mRNAs of four classifications (hyper-up, hyper-down, hypo-up and hypo-down) are shown in Table 1. Finally, we achieved synchronous functional analysis of four classifications via Metascape. Regulation of cellular response to stress and Nervous system development were the shared Enriched Ontologies (Fig. 7 and Supplement Figure 3). Moreover, a few of annotations related to stone development were also significantly enriched, including cell junction organization, immune system development, regulation of cell adhesion, cellular response to DNA damage stimulus and cell cycle in hyper-up cluster, cytokine signaling in immune system, regulation of apoptotic signaling pathway, regulation of ion transport, cell proliferation, response to oxidative stress and signaling by NOTCH in hypo-down cluster.

Discussions

m6A RNA methylation is the most abundant mRNA modification and has emerged as a crucial gene expression regulatory mechanism related to cellular differentiation, development and cancer progression. Unlike with DNA methylation, RNA methylation takes place at post-transcriptional levels and m6A-tagged mRNAs can be recognized by "readers", which in turn influences the fate of mRNAs on mRNA splicing, translation, stability and degradation [12]. Although RNA methylation has become the current hot topic, the relationship between m6A and urinary calculi is still a blank field. To make up for gaps, we implemented the first transcriptome-wide m6A mapping study on kidney injury induced by CaOx crystals.

Dysregulation of m6A methylation has been discovered in many pathologic processes of disease. Mathiyalagan et al. [9] reported that increased m6A levels were detected in human failing hearts, and myocardial FTO demethylase gene transfer rescued cardiac function in mouse models of myocardial infarction. Chen et al. [13] reported a negative association between m6A and autophagy in Leydig cells during testosterone synthesis and provided new insights for treating azoospermatism by exploiting m6A regulation. Niu et al. [14] found that demethylase FTO sustained the lower

Table 1 Top 10 m6A foldchange mRNAs of four classifications

Transcript_ID	Foldchange (GE)	Foldchange (m6A)	transcript_type	GeneSymbol	Expression		Methylation		Cluster
					CaOX (mean)	Control (mean)	CaOX (mean)	Control (mean)	
ENST00000480716	170.7496908	99.62003186	protein_coding	ZNF169	–1.795584525	–3.185751762	–2.207082167	–4.432132142	hyper-up
ENST00000258955	167.2254742	27.39023984	protein_coding	RSAD1	1.966227341	0.724085984	1.497566199	0.388937682	hyper-up
ENST00000538570	140.2967673	145.0297978	protein_coding	COL4A6	–1.531194716	–3.124689802	–2.383793392	–3.949561666	hyper-up
ENST00000421093	130.9699679	81.6623387	protein_coding	ZNF219	8.364693665	6.292583395	8.120614889	5.250738681	hyper-up
ENST00000436346	125.8155822	28.38959706	protein_coding	CCDC88A	–0.191398162	–1.623477778	–0.579375927	–1.869505322	hyper-up
ENST00000327245	124.2118616	61.21306366	protein_coding	ATP10B	7.983260975	3.480469875	7.426468979	2.978581272	hyper-up
ENST00000366974	118.9549863	12.89991711	protein_coding	TATDN3	–1.254993485	–2.968346039	–2.73138256	–4.057260311	hyper-up
ENST00000367889	107.9160564	94.75236522	protein_coding	MGST3	–2.226968101	–3.477552252	–2.998376045	–5.27308748	hyper-up
ENST00000305264	106.8491827	159.4152739	protein_coding	HDAC3	4.48615441	0.877213174	1.92709138	0.359047162	hyper-up
ENST00000236957	103.0441968	39.27252924	protein_coding	EEF1B2	–0.475140637	–2.285490028	–0.926193579	–3.396942907	hyper-up
ENST00000409320	0.20168857	2.074814952	protein_coding	RPL31	5.808176467	8.117975239	4.765298983	3.712316312	hyper-down
ENST00000316084	0.27866858	2.496379586	protein_coding	RPS4X	–2.159871416	–1.078320487	–2.612036873	–4.00249333	hyper-down
ENST00000476941	0.308830762	2.168020111	protein_coding	TRPC1	–2.823897277	–1.608710166	–3.129916464	–4.214987036	hyper-down
ENST00000398606	0.337636546	2.572313341	protein_coding	GSTP1	6.806877164	8.165824528	6.063049484	4.275746467	hyper-down
ENST00000311672	0.349867616	2.435654695	protein_coding	UQCRH	7.422353733	8.878016997	4.451809329	3.160321927	hyper-down
ENST00000377803	0.364587432	2.447802911	protein_coding	HIST1H4C	–0.909702345	0.605416615	–1.268815159	–2.553124775	hyper-down
ENST00000239666	0.377646133	2.004587049	protein_coding	PDZD11	–2.42867265	–1.14361716	–2.706248776	–4.082850595	hyper-down
ENST00000369081	0.382030615	2.280191295	protein_coding	INPP5F	–2.33867035	–0.954392861	–2.810394067	–3.874601603	hyper-down
ENST00000468812	0.383081301	2.091020978	protein_coding	PPIA	–1.686601399	–0.681935138	–2.140974013	–3.198423217	hyper-down
ENST00000336023	0.389866645	3.451690279	protein_coding	TUBA1B	–0.989816735	0.021011657	–1.628001772	–2.677621041	hyper-down
ENST00000400588	13.37047991	0.439487121	protein_coding	GAB4	4.106149314	1.184970192	–2.102360692	0.544543246	hypo-up
ENST00000348547	13.36887385	0.417730285	protein_coding	ERGIC3	3.44513396	0.242347073	–1.574092714	–0.273231244	hypo-up
ENST00000393306	13.35868452	0.44634189	protein_coding	OSGIN1	3.122298963	–0.179469193	–2.319332223	–0.950419688	hypo-up
ENST00000407936	12.43662761	0.350856546	protein_coding	POLR2F	0.972654067	–0.85048839	–2.742189286	–1.710123553	hypo-up
ENST00000320521	12.33079497	0.34937181	protein_coding	SLC16A8	0.20007158	–1.744512767	–4.530005454	–2.442401739	hypo-up
ENST00000396992	12.18976899	0.432589785	protein_coding	CFP	1.101354175	–0.055942414	–2.014773463	–0.864130964	hypo-up
ENST00000374900	12.1066743	0.324086258	protein_coding	FAAH2	0.577596414	–1.081411374	–4.382735093	–1.873754693	hypo-up
ENST00000606370	12.09098888	0.475949383	protein_coding	TBC1D7	1.098004097	–0.950608149	–3.074459794	–1.749832721	hypo-up
ENST00000453001	11.47597606	0.345892054	protein_coding	PPP2R2B	0.224630075	–1.026582043	–4.059682525	–1.617450464	hypo-up
ENST00000397572	10.99913072	0.281439469	protein_coding	MYCBP	2.322949799	–0.79677764	–2.461777987	–1.445522424	hypo-up
ENST00000533076	0.002458385	0.039564424	protein_coding	SLC39A13	2.198936205	4.408673979	–0.33702268	1.549406275	hypo-down
ENST00000593490	0.003732658	0.033516402	protein_coding	KLK8	–1.98738672	–0.083031485	–2.778463607	–1.63742506	hypo-down
ENST00000307616	0.003786078	0.054521483	protein_coding	C11orf40	–0.953146141	1.54316292	–1.514973691	–0.119903477	hypo-down
ENST00000354884	0.004144895	0.029113351	protein_coding	SLC39A13	–0.462043536	1.542169295	–0.965006249	0.110607368	hypo-down
ENST00000536005	0.005635406	0.010247727	protein_coding	BEAN1	–2.309468188	0.670631116	–2.959489497	–1.824249284	hypo-down
ENST00000619644	0.00634611	0.032616225	protein_coding	SMTN	0.388898017	2.271867946	–1.076072825	–0.049952978	hypo-down
ENST00000602198	0.006368568	0.015412417	protein_coding	TEX101	–0.104842067	2.409857831	–1.060248487	1.062600468	hypo-down
ENST00000335793	0.006700264	0.022083641	protein_coding	CDC42EP4	–2.665717838	1.674459116	–3.268228074	–1.679864524	hypo-down
ENST00000450366	0.007749304	0.075163656	protein_coding	LANCL1	4.738020273	5.755884107	4.346765081	5.423398303	hypo-down
ENST00000546300	0.007855529	0.089022621	protein_coding	GPR161	1.073151046	3.619340473	–0.009668707	1.596001274	hypo-down

m6A levels of breast tumor and induced the degradation of BNIP3 (a pro-apoptosis gene), which mediated tumor growth and metastasis. In our study, we observed that intracellular overall m6A modification was up-regulated when being stimulated by CaOx crystals. And this phenomenon could only be explained by the down-regulation of demethylase FTO. This section indicated that m6A was involved in the process of crystal-cell interaction, while the key role of FTO was required to be further investigated. For other regulators, we found the unmatched results between qPCR and Western Blot, and it can be explained that the process of translation might be regulated by other mechanisms and the expression levels were also affected by different inducing conditions.

Increased intracellular generation of reactive oxygen species (ROS) can cause DNA damage and cell apoptosis [15]. High concentrations of CaOX crystals can induce oxidative stress and inflammation, and accelerate CaOX stone formation by mediating renal tubular apoptosis and crystal–cell adhesion [16, 17]. Furthermore, the functional impairment of tubular reabsorption and secretion disturbs molecular homeostasis in the tubules and promotes the supersaturation of stone-forming

substances. Yu et al. [18] reported that demethylase ALKBH5 protected cells from DNA damage and apoptosis via modulating m6A modifications related to DNA repair process during ROS-induced stress. In our study, we found that m6A dysregulation had widespread influence on molecular metabolism and various cellular processes, indicating the internal complicated mechanisms of cellular response to crystalline injury. Our differentially methylated results demonstrated that herpes simplex virus 1 infection was identified as the main enrichment pathway of differential up-regulated and hypermethylated genes. Besides viral proteins, we noticed that pro- and anti-apoptotic genes were also enriched in this pathway such as Fas, Bax, Bcl-2, CASP8, BIRC2 and BIRC3, etc. Meanwhile, we found that both hypermethylated and hypomethylated genes could be enriched in apoptosis pathway. In addition to apoptosis, we also noticed that nucleotide excision repair and mismatch repair were enriched in hypermethylated genes. In the field of crystal–cell interaction, the relationship of oxidative stress to cellular injury has been most frequently investigated, and we explored the underlying mechanisms afresh at the post-transcriptional levels.

In conjoint analysis, we filtered out these genes without differential expression and differential methylation between the two omics and obtained four classifications as described above. As expected, the functional analysis indicated that m6A methylation regulated the expression of those genes associated with response to DNA damage, immune system and apoptosis. Besides these, two gene sets (cell junction and cell adhesion) should also be stressed. Cellular tight junction in the tubular cells serves as a "paracellular barrier" to limit the passage of ions and pathogens, and maintain the cell polarity and physiological function, and Peerapen et al. [19] reported that CaOX crystals could lead to tight junction disruption in distal tubular epithelial cells via p38 MAPK activation. Crystal–cell adhesion is another key point in the onset and progression of stone formation. Qi et al. [20] showed that adhesion molecules (osteopontin, hyaluronic acid and CD44) were up-regulated in CaOX-treated cells. In our study, we observed that these two gene sets (regulation of cell adhesion and cell junction organization) were also significantly enriched in three clusters, including hyper-up, hypo-up and hypo-down. These results revealed that m6A methylation exerted great impact on the development of CaOX through participating multiple processes covering inflammation, oxidative stress, apoptosis, crystal–cell adhesion, etc.

Conclusions

We delineated the first transcriptome-wide m6A landscape of injurious renal tubular cells in high CaOX environment via microarray analysis. We identified a series of mRNAs of renal tubular epithelial cells with differential expression and m6A methylation between the CaOX-treated groups and controls. In addition, we uncovered the underlying mechanisms by which m6A methylation regulated crystal-cell interaction and tubular cellular injury induced by CaOX.

Supplementary Information The online version contains supplementary material available at https://doi.org/10.1007/s00240-023-01425-7.

Author contributions B-YY and F-ZZ conceptualized the study.F-ZZ, B-YY, JL designed the study, carried out the statistical analyses, reviewed and revised the manuscript.B-YY and F-ZZ wrote the paper.X-CW, H-MZ and YT coordinated and supervised data collection, critically reviewed and revised the manuscript.All the authors approved the final manuscript as submitted.

Funding This study was funded by Beijing Municipal Administration of Hospitals Clinical medicine Development of special funding support, code: 2022–2-1102; National Natural Scientific Foundation of China (Grant No. 82002711); Beijing Municipal Administration of Hospitals' Youth Programme (Code: QML20200105).

Declarations

Ethical approval Ethical approval was not required in this study.

Conflict of interest The authors declare that they have no conflict of interest.

Informed consent Informed consent was not required in this study.

References

1. Denburg MR, Koepsell K, Lee JJ, Gerber J, Bittinger K, Tasian GE (2020) Perturbations of the gut microbiome and metabolome in children with calcium oxalate kidney stone disease. J Am Soc Nephrol 31:1358–1369
2. Khan SR, Canales BK, Dominguez-Gutierrez PR (2021) Randall's plaque and calcium oxalate stone formation: role for immunity and inflammation. Nat Rev Nephrol 17(6):417–433
3. Jiang K, Hu J, Luo G, Song D, Zhang P, Zhu J, Sun F (2020) miR-155–5p promotes oxalate- and calcium-induced kidney oxidative stress injury by suppressing MGP expression. Oxid Med Cell Longev 2020: 5863617
4. Zhu W, Zhao Z, Chou FJ, Zuo L, Liu T, Bushinsky D, Chang C, Zeng G, Yeh S (2019) The protective roles of estrogen receptor β in renal calcium oxalate crystal formation via reducing the liver oxalate biosynthesis and renal oxidative stress-mediated cell Injury Oxid Med Cell Longev 2019:5305014
5. Liu XM, Zhou J, Mao Y, Ji Q, Qian SB (2019) Programmable RNA N(6)-methyladenosine editing by CRISPR-Cas9 conjugates. Nat Chem Biol 15:865–871
6. Oerum S, Meynier V, Catala M, Tisné C (2021) A comprehensive review of m6A/m6Am RNA methyltransferase structures. Nucleic Acids Res 49:7239–7255
7. Zhang H, Shi X, Huang T, Zhao X, Chen W, Gu N, Zhang R (2020) Dynamic landscape and evolution of m6A methylation in human. Nucleic Acids Res 48:6251–6264
8. Wang X, Ma R, Zhang X, Cui L, Ding Y, Shi W, Guo C, Shi Y (2021) Crosstalk between N6-methyladenosine modification and

circular RNAs: current understanding and future directions. Mol Cancer 20: 121
9. Mathiyalagan P, Adamiak M, Mayourian J, Sassi Y, Liang Y, Agarwal N, Jha D, Zhang S, Kohlbrenner E, Chepurko E, Chen J, Trivieri MG, Singh R, Bouchareb R, Fish K, Ishikawa K, Lebeche D, Hajjar RJ, Sahoo S (2019) FTO-Dependent N(6)-Methyladenosine Regulates Cardiac Function During Remodeling and Repair. Circulation 139:518–532
10. Yu J, Zhang Y, Ma H, Zeng R, Liu R, Wang P, Jin X, Zhao Y (2020) Epitranscriptomic profiling of N6-methyladenosine-related RNA methylation in rat cerebral cortex following traumatic brain injury. Mol Brain 13: 11
11. Wang Z, Li MX, Xu CZ, Zhang Y, Deng Q, Sun R, Hu QY, Zhang SP, Zhang JW, Liang H (2020) Comprehensive study of altered proteomic landscape in proximal renal tubular epithelial cells in response to calcium oxalate monohydrate crystals. BMC Urol 20:136
12. Zaccara S, Ries RJ, Jaffrey SR (2019) Reading, writing and erasing mRNA methylation. Nat Rev Mol Cell Biol 20:608–624
13. Chen Y, Wang J, Xu D, Xiang Z, Ding J, Yang X, Li D, Han X (2021) m(6)A mRNA methylation regulates testosterone synthesis through modulating autophagy in Leydig cells. Autophagy 17:457–475
14. Niu Y, Lin Z, Wan A, Chen H, Liang H, Sun L, Wang Y, Li X, Xiong XF, Wei B, Wu X, Wan G (2019) RNA N6-methyladenosine demethylase FTO promotes breast tumor progression through inhibiting BNIP3. Mol Cancer 18: 46
15. Yan Q, Chen Y, Liu H, Li G, Liang C, Hao Z (2022) Effects of alternative splicing events and transcriptome changes on kidney stone formation. Urolithiasis 50(2):131–140
16. Sun Y, Kang J, Guan X, Xu H, Wang X, Deng Y (2021) Regulation of endoplasmic reticulum stress on the damage and apoptosis of renal tubular epithelial cells induced by calcium oxalate crystals. Urolithiasis 49:291–299
17. Patel M, Yarlagadda V, Adedoyin O, Saini V, Assimos DG, Holmes RP, Mitchell T (2018) Oxalate induces mitochondrial dysfunction and disrupts redox homeostasis in a human monocyte derived cell line. Redox Biol 15:207–215
18. Yu F, Wei J, Cui X, Yu C, Ni W, Bungert J, Wu L, He C, Qian Z (2021) Post-translational modification of RNA m6A demethylase ALKBH5 regulates ROS-induced DNA damage response. Nucleic Acids Res 49:5779–5797
19. Peerapen P, Thongboonkerd V (2013) p38 MAPK mediates calcium oxalate crystal-induced tight junction disruption in distal renal tubular epithelial cells. Sci Rep 3: 1041
20. Qi S, Wang Q, Xie B, Chen Y, Zhang Z, Xu Y (2020) P38 MAPK signaling pathway mediates COM crystal-induced crystal adhesion change in rat renal tubular epithelial cells. Urolithiasis 48:9–18